# The emplacement model of the Qitianling pluton in southern Hunan, China: New insights from 3-D magnetotelluric imaging

Zhou, Keke; Liu, Jianxin; Guo, Rongwen; Comeau, Matthew J.; Liu, Rong; Cao, Chuanghua; Zou, Guangjun; Li, Jian; Wang, Yongfei

**DOI**
10.1016/j.oregeorev.2025.106511

**Publication date**
2025

**Document Version**
Final published version

**Published in**
Ore Geology Reviews

Ore Geology Reviews 180 (2025) 106511

Contents lists available at ScienceDirect

Ore Geology Reviews

journal homepage: www.elsevier.com/locate/oregeorev

# The emplacement model of the Qitianling pluton in southern Hunan, China: New insights from 3-D magnetotelluric imaging

Keke Zhou [a,b,c], Jianxin Liu [a,b,c,*], Rongwen Guo [a,b,c], Matthew J. Comeau [d], Rong Liu [a,b,c], Chuanghua Cao [e,*], Guangjun Zou [e], Jian Li [b,f], Yongfei Wang [g]

[a] School of Geosciences and Info-Physics, Central South University, Changsha 410083, China
[b] Hunan Key Laboratory of Nonferrous Resources and Geological Hazards Exploration, Changsha 410083, China
[c] Key Laboratory of Metallogenic Prediction of Nonferrous Metals and Geological Environment Monitoring (Central South University), Ministry of Education, Changsha 410083, China
[d] Department of Geoscience and Engineering, Delft University of Technology, 2628 CN Delft, Netherlands
[e] Geological Bureau of Hunan Province, Changsha 410011, China
[f] Faculty of Geosciences and Engineering, Southwest Jiaotong University, Chengdu 611756, China
[g] Department of Mathematical Sciences, Tsinghua University, Beijing 100084, China

ARTICLE INFO

*Keywords:*
Magma emplacement
Electrical resistivity
Qitianling pluton
South China
Metallogenesis

ABSTRACT

The Qitianling pluton in southern Hunan, China, has spatially and genetically influenced the formation and distribution of a series of polymetallic deposits, including Xintianling, Baoshan, Huangshaping, and Furong. These deposits host a variety of tungsten- and tin-related deposits, often regarded as strategic and critical rare metals, and comprise one of the most prominent reserves globally. A thorough understanding of the structure of the Qitianling pluton is essential for insights into the development and evolution of the metallogenic system in southern Hunan. Working towards the goal of investigating regional structural features and magma emplacements model, we have generated three-dimensional (3-D) electrical resistivity models of the Qitianling pluton and its surrounding areas to upper-crustal depth using magnetotelluric (MT) data that range from 1000 Hz to 0.001 Hz. The results reveal that the upper-crust of southern Hunan is mainly characterized by high resistivity with multiple unique conductive zones. The high-resistivity anomalies ($>$ 1000 Ω·m) are interpreted to represent the Qitianling pluton. In addition, they correspond very well to a negative residual Bouguer gravity anomaly. Moreover, the morphology of the feature aligns with low-velocity obtained by modelling reflected seismic waves. Conductive anomalies ($<$ 30 Ω·m) near the sides of the pluton that extend through the upper crust likely indicate the presence of the Chenzhou-Linwu deep-seated fault system, which may have served as a pathway for the upward migration and emplacement of magma/hydrothermal fluids. Conductive features ($<$ 30 Ω·m) beneath the Qitianling pluton are inferred to represent ancient magma reservoirs where assimilation and mixing processes occurred before magma emplacement. Based on the geophysical models and the available geological data, a multi-stage magma emplacement model of the Qitianling pluton is proposed, which provides new insights into the W-Sn polymetallic mineralization system and the regional magmatic evolution within southern Hunan.

## 1. Introduction

Tungsten and tin are both regarded as rare metals with strategic importance, due to economic and supply chain reasons, and are widely used in various industrial fields including electronic communication, photoelectric materials, energy materials, and aerospace (Yuan et al., 2019; Chen et al., 2015; Mao et al., 2013). Currently, the reserves of tungsten and tin resources in the Nanling Range, South China, account for more than 50 % and about 20 %, respectively, of the global total, making them the largest in the world (Yin et al., 2021; Yuan et al., 2019). However, following the continuous exploration and exploitation of near-surface mineral resources, the supply of accessible reserves is becoming progressively insufficient (Li et al., 2018). To meet the growing demand for tungsten and tin production driven by rapid societal and economic developments, deep prospecting based on reliable exploration technology in unexplored or under-explored regions has

* Corresponding authors at: School of Geosciences and Info-Physics, Central South University, Changsha 410083, China (J. Liu).
*E-mail address:* ljx@csu.edu.cn (J. Liu).

https://doi.org/10.1016/j.oregeorev.2025.106511
Received 21 November 2024; Received in revised form 12 February 2025; Accepted 20 February 2025
Available online 28 February 2025

become a crucial research topic (Qu et al., 2020; Dentith et al., 2018).

The W-Sn polymetallic concentration area of southern Hunan, China, located in the northern margin of the central part of the Nanling Range, is renowned as one of the most prominent W-Sn-producing districts in China (Mao et al., 2013). This area accounts for a significant part of global tungsten resources and contains substantial tin and rare metal deposits (Yuan et al., 2019). Particularly, the Qitianling pluton and its surrounding region host a variety of W- and Sn-related polymetallic deposits, such as the Xintianling W-Mo deposit, the Shizhuyuan W-Sn-Mo-Bi-F deposit, the Yaogangxian W-Mo deposit, the Furong Sn deposit and the Xianghualing Sn-W-Pb-Zn deposit (Xie et al., 2010; Li et al., 2014). Previous studies involving geological structures, geochemistry, geochronology, and geophysics have revealed the deep prospecting potential of this region (Mao et al., 2013; Li et al., 2018; Yin et al., 2021; Yuan et al., 2022), and some significant pieces of evidence supporting this possibility have been recorded, as follows.

Favorable deep structures and crustal architecture (e.g., deep-seated faults) have developed in the southern Hunan area, playing a vital guiding role in the transportation of ore-forming fluids and the discrete emplacement of deposits (Yuan et al., 2022; Sheng et al., 2023). In this area these mainly include the northeast-trending Chenzhou-Linwu fault (CLF) and the northwest-trending Chenzhou-Shaoyang strike-slip fault (CSF) (Li et al., 2018). Furthermore, the Mesozoic granitic rocks, widely exposed, provided abundant ore-forming materials for mineralization at depth, which aligns with the theoretical system for (large) deposits formed by smaller intrusions put forward by Tang et al. (2015). Interestingly, substantial deep prospecting discoveries based on known deposits have recently been made in the region, including the multi-layer mineralized bodies that have been revealed at a depth of about 2 km in the Ping-Bao district (Dai et al., 2023). The above knowledge indicates that the W-Sn polymetallic concentration area of southern Hunan has favorable deep metallogenic conditions and high exploration potential. Therefore, knowledge of the spatial distribution of ore-controlling structures is crucial for gaining a better understanding of the development and evolution of the mineral system (e.g., Dentith et al., 2018; Comeau et al., 2021; Comeau et al., 2022).

However, the existing prospecting research carried out in the southern Hunan area has mainly focused on near-surface or micro-scale structural features, such as petrology, mineralogy, surface geology, petrophysics, and radiometric dating (Liu et al., 2018; Huang et al., 2019; Chen et al., 2022). In addition, while gravity modeling of density contrasts has been used to delineate the horizontal boundaries of the major granitoid intrusions in this area, its limited vertical resolution hampers the accurate imaging of deep structures (Liu et al., 2023). Simply put, inadequate deep exploration is likely to result in a limited understanding of deep structures, therefore the use of deep exploration technology is essential for this research.

Magnetotelluric (MT) exploration, proposed in the 1950's (Cagniard, 1953; Tikhonov, 1950), is a passive electromagnetic method that enables imaging the electrical resistivity of the subsurface at multiple spatial scales and depths (e.g., Chave et al., 2012; Jin et al., 2022; Sheng et al., 2022; Wang et al., 2024). Because of its high detection depth, the MT method has recently been widely employed in deep resource exploration, utilizing the varied resistivity properties between the surrounding rocks and the exploration targets, e.g., minerals and/or geothermal fluids, (e.g., Hill et al., 2015; Heinson et al., 2018; Guo et al., 2020; Lü et al., 2021; Comeau et al. 2022; Sheng et al., 2022, 2024; Liu et al., 2023).

There is a consensus that the subsurface structures of South China are mainly controlled by multi-stage tectonic-magmatic events (Mao et al., 2013). These structures have a direct impact on the formation and transportation of ore-forming fluids to near-surface depths (e.g., Comeau et al., 2021). Therefore, the upper-crustal framework inferred from 3-D resistivity models can give valuable insight into the formation and development of the mineral system. In this paper, a high-density MT array, consisting of two long lines, was deployed across the Qitianling pluton and its surrounding region (Line1 and Line2; Fig. 1). We developed 3-D electrical resistivity models for the upper crust of this key region of southern Hunan. Combining our results with geological data and with other geophysical data, we investigate the main structural features and propose a multi-stage magmatic emplacement model for the Qitianling pluton. The new findings provide reliable electrical resistivity constraints for a better understanding of the deep extension of ore-controlling structures, polymetallic mineralization systems, as well as regional magmatic evolution. Furthermore, it will play a crucial role in scientifically guiding the research of deep prospecting and exploration within the W-Sn polymetallic ore concentration area of southern Hunan.

## 2. Regional background

The South China Block (SCB) was formed as part of the supercontinent Rodinia (e.g., Cawood et al., 2013; Xu et al., 2019, 2023), through the amalgamation of the Yangtze Block (YZB) and Cathaysia Block (CB) along the Jiangnan orogenic belt (JNO) about 1.1–0.83 Ga (e.g., Zhao et al., 2011, 2012; Mao et al., 2013; Faure et al., 2016; Yuan et al., 2019). During the Neoproterozoic, the breakup of Rodinia, driven by continental extension, led to extensive structural reworking in South China (e.g., Xu et al., 2019, 2023). Synchronous magmatic events, typically represented by the Paleozoic and Mesozoic orogenies and the Late Mesozoic subduction of the Paleo-Pacific plate (e.g., Faure et al., 2014; Shu et al., 2011), contributed to the formation of the west-east trending Nanling Range (e.g., Yuan et al., 2019; Yin et al., 2021). Voluminous upwelling of magma and mantle-crust interaction gave rise to widespread emplacement of W-Sn polymetallic deposits in the Nanling Range, mainly between 160 and 150 Ma with a peak at ~ 156 Ma (e.g., Hu et al., 2017; Ni et al., 2023). According to Yin et al. (2021), W-Sn deposits are the results of the northwestward subduction of the Izanagi slab beneath the Eurasia plate starting at ~ 175 Ma. On the other hand, the heterogeneity of the distribution of the W-Sn-related deposits in the Nanling Range can be attributed to several factors, such as the different melting temperatures of the granitic protoliths in the source area (e.g., Yuan et al., 2019), contrasting magmatic histories (Cheng et al., 2018), and distinct paths of metal redistribution (Schmidt, 2018).

The southern Hunan area within the interior of the Nanling Range mainly experienced two stages of W-Sn mineralization events, namely the Jurassic and the Cretaceous, which coincided with that of the South China Block (e.g., Mao et al., 2013, 2018). The Jurassic mineralization occurred under an inland back-arc extensional setting which was triggered by subduction, and then another mineralization event took place during the Cretaceous along the continental margin, induced by post-subduction processes (e.g., Mao et al., 2018). The Jurassic mineralization is most closely associated with the W-Sn deposits in the southern Hunan area (Zhu et al., 2009). As the most important ore-controlling structure in the southern Hunan area, the crust-scale CLF system played an important role in the transport of upwelling ore-bearing magma originating from the mantle (Li et al., 2014). This fault, however, had no effect on the composition and distribution of the metamorphic basement in the Nanling region as it formed before the basement (Yuan et al., 2019). In addition, the region is characterized by Devonian, Carboniferous, Permian, Triassic, and Jurassic strata, with lamprophyre dikes intruded into these strata. Other rock types distributed in the area include limestone, mudstone, and sandstone (Mao et al., 2013).

Importantly, the granitic Qitianling pluton is considered the ultimate product of magmatic evolution in the southern Hunan area forming at around 146–163 Ma (Zhu et al., 2009), and covering an area of ~ 530 $km^2$ (He et al., 2014; Liu et al., 2018). There is a consensus that the magma emplacements associated with this pluton can be categorized into three main stages (Zhu et al., 2009; Li et al., 2014). The first stage occurred between 160 and 163 Ma, its lithology is predominantly composed of amphibole-biotite-rich monzonitic granite with ~ 45 % of the exposure. The second stage dated 153–157 Ma, mainly comprises

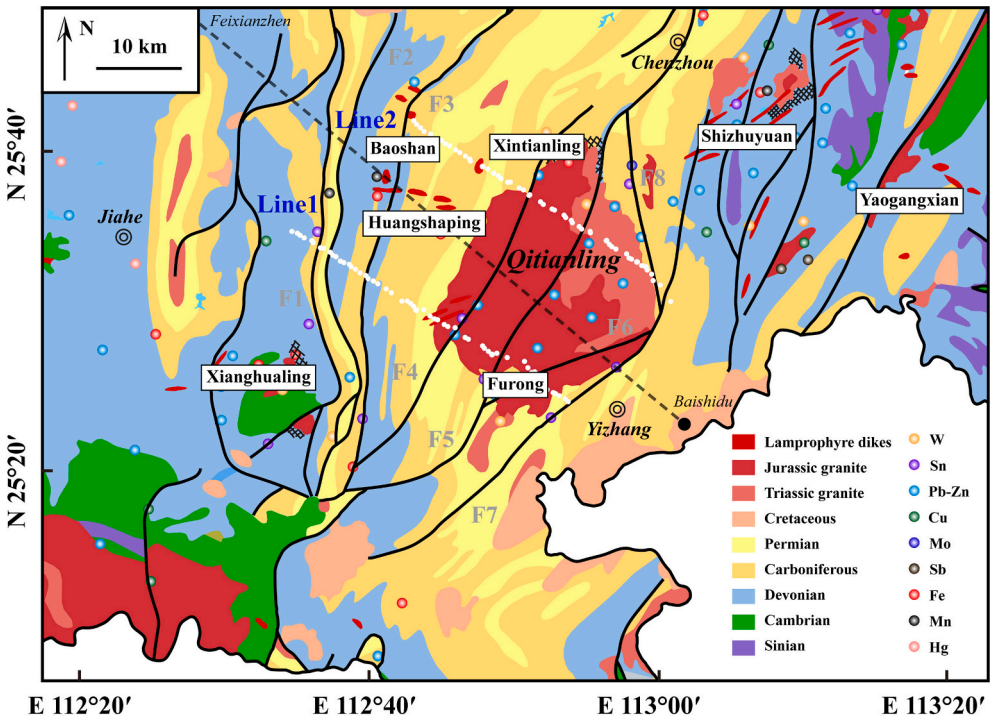


**Fig. 1.** Geological sketch map of southern Hunan, modified from Li et al. (2021), showing the distribution of granitic intrusions and related polymetallic deposits. The magnetotelluric (MT) measurement locations, in two long lines, are depicted as white dots. The location of deposits are indicated with colored circles. The gray dashed line represents the reflected seismic profile obtained from Li et al. (2014). The black solid lines represent the secondary faults affiliated with the Chenzhou-Linwu fault system (CLF), labeled as F1-F8, and the black grid lines represent the working mining districts.

biotite ± amphibole-bearing granite, covering about 40 % of the emerging area (Liu et al., 2018). Lastly, the magma intruded into the above two granite facies in the form of supplementary intrusions during 146–150 Ma, which led to fine-grained biotite-bearing granite, accounting for about 15 % of the pluton exposure (Liu et al., 2018; Huang et al., 2019). Since the Qitianling pluton served as the mineral source and energy supply for W-Sn mineralization in southern Hunan, an adequate understanding of its emplacement process is essential to unlock the deep metallogenic potential of the W-Sn mineral system.

## 3. Data and method

### 3.1. Data collection and analysis

Magnetotelluric (MT) data are composed of electric and magnetic fields measurements, carried out at the surface of the Earth, and associated by a transfer function known as the impedance tensor (**Z**) that is sensitive to the Earth's subsurface electrical resistivity and from which we can compute the apparent resistivity and impedance phase (Chave et al., 2012). In this study, a total of 113 MT measurements (white dots in Fig.1) were collected forming an array consisting of two long lines spanning the Qitianling pluton and its surrounding region. Specifically, Line 1 and Line 2 are composed of 59 and 54 MT measurements, respectively, with a minimum spacing of ~ 500 m and an average spacing of ~ 1500 m. The line length is ~ 38 km and the line separation distance is about 17 km, arranged in parallel along NW57°. Additionally, the apparent resistivity and phase pseudo sections, presenting the original data have been plotted, as shown in Fig.2. They play an important role in evaluating the inversion results and subsequent geological interpretation.

The MT data were collected with wide band magnetotelluric instruments developed by GSAI Geophysics (https://www.gs-ait.com). During data acquisition, multiple instruments simultaneously recorded four components of the electromagnetic field ($E_x$, $E_y$, $H_x$, $H_y$) at the surface. The axes were orthogonal, orientated with $x$ to the north, $y$ to the east, and $z$ vertically downward. The recording time at each MT measurement site was approximately one day, giving responses within the period range of 0.001–1,000 s.

The collected raw data were processed with GSEM-PROS software. This software converts time series data to the frequency domain and obtains sounding curves of the apparent resistivity and impedance phase at the corresponding MT measurement locations. As a result of the dense population and industry in the survey area, much of the MT data were disturbed by cultural electrical noise, especially those near wind turbines and mining enterprises. Therefore, we use both remote referencing (Chave et al., 2012; McNeice & Jones, 2001; Gamble et al., 1979) and local referencing techniques (Mao et al., 2021). These methods help recover noise-affected data, increasing the amount of usable data. To ensure the reliability of the generated resistivity models, a subset of the data that was deemed to be acceptable quality was selected and used for subsequent analysis and inversion calculations.

### 3.2. Dimensionality analysis

Detailed dimensionality analysis should be carried out before inversion and interpretation, due to its crucial role in evaluating the complexity of subsurface structures and the distortion degree of the MT data. In this study, two methods, namely the Groom-Bailey (G-B) impedance tensor decomposition (Groom and Bailey, 1989) and the phase tensor analysis (Caldwell et al., 2004; Booker, 2014), were implemented to extract insights into the dimensionality and geoelectric strike direction. As shown in Figs. 3 and 4, the geoelectric strike direction and phase tensor are plotted at various periods, which gives information at different depths, based on the concept of skin depth (Chave et al., 2012).

In the Qitianling region, the phase tensors for all period bands show both small and large absolute skew values and both small and large apparent ellipticity, indicating 3-D electrical structures exist in parts of

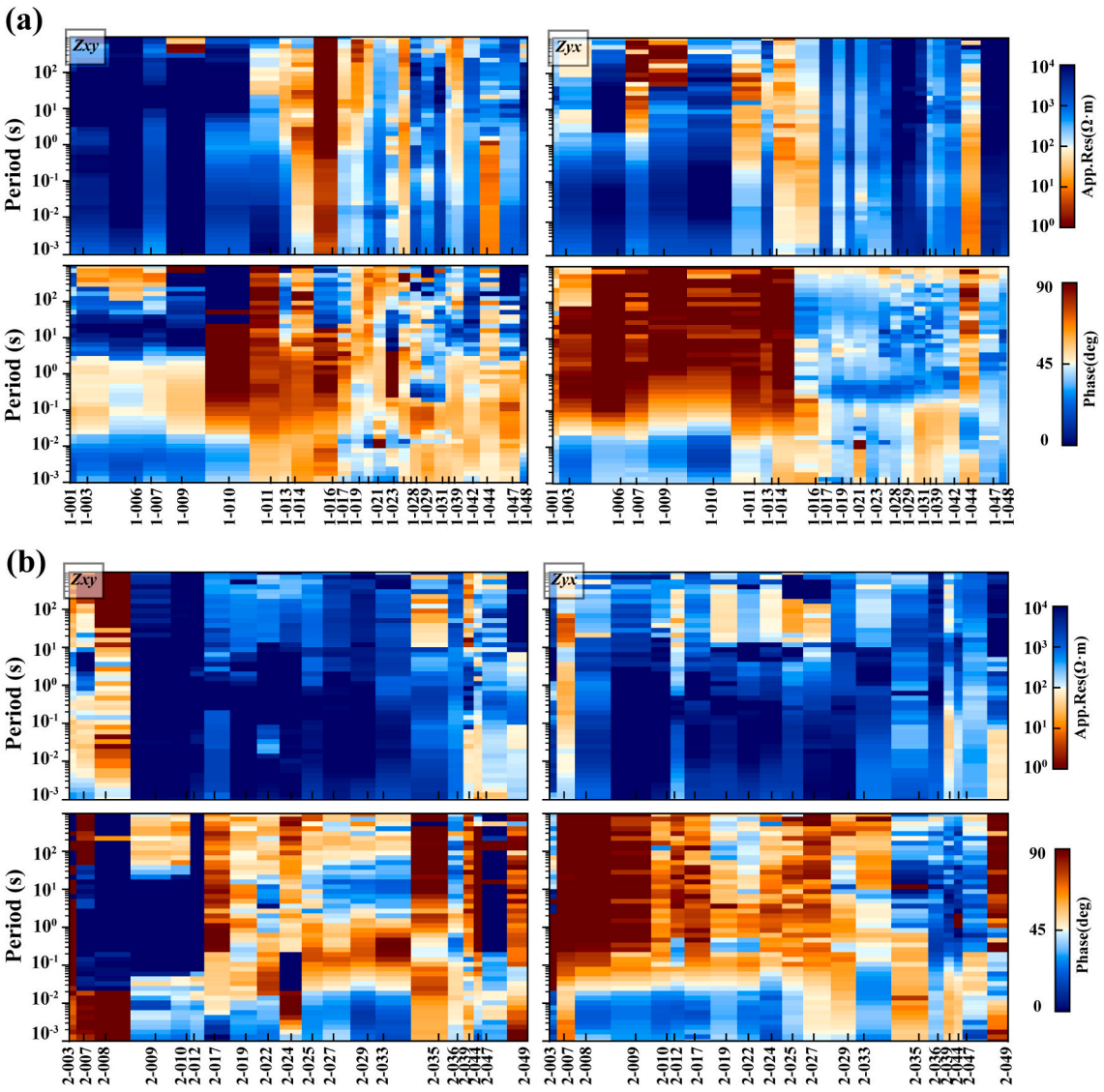


**Fig. 2.** The apparent resistivity and phase pseudo sections. (a) Line 1; (b) Line 2.

the data. The major-axis direction is NWW-SEE, aligning with, or being perpendicular to, the regional geological strike directions, as indicated by rose diagrams derived from G-B tensor decomposition (see Fig. 4). This is consistent with previous regional analyses (Yin et al., 2021). The phase tensor results near fault zones show relatively complex directionality and large skew values, suggesting significant 3-D features consistent with the variable strike directions in the G-B rose diagrams. Moreover, for most MT sites, especially in the longer-period range of about $>$ 10 s where pronounced elliptical polarization occurs, the skew angles exceed 3°, which suggests that performing a 3-D inversion is more appropriate for the accurate interpretation of these data.

### 3.3. Three-dimensional inversion

The MT data (off-diagonal and diagonal components) were inverted with the ModEM inversion algorithm based on the nonlinear conjugate gradient (NLCG) algorithm (Egbert and Kelbert, 2012; Kelbert et al., 2014), generating 3-D electrical resistivity models. Given the large separation between profiles (~ 17 km) with the small measurement site spacing, separate models were created for these two lines, enabling much finer discretization of the modeling grid resulting in more information than a single regional-scale model (Comeau et al., 2021). Moreover, this modeling approach facilitated enhanced resolution of intricate structural details, enabling faster and smoother convergence.

Similar model parameters were adopted for the two regions. The error floors of 10% and 5% of $|\boldsymbol{Z}_{xy}\cdot\boldsymbol{Z}_{yx}|^{1/2}$ were assigned to diagonal and off-diagonal components of the impedance tensor, respectively. Focusing on the upper crust, from surface to 10 km depth, MT data within the frequency range of 1000 Hz (sensitive to shallow regions) to 0.1 Hz (sensitive to deeper regions) is sufficient for our exploration targets (based on skin depth calculations). The starting model was a homogenous half-space with a resistivity value of 100 Ω·m, and no topography was included in the models. The research area was discretized using a grid with 500 m horizontal spacing in the central area, padded with 10 cells on each edge, expanding outward by a factor of 1.5 to the model boundary. Vertically, 60 layers were set, starting with a thickness of 5 m and increasing geometrically with a factor of 1.2, to enable detailed imaging of fine upper-crustal structures. The total number of grid cells differed slightly between the models, the discretization along Line 1 resulted in a 61 × 82 × 60 grid cells in the $x$, $y$, and $z$ directions respectively, while the one related to Line 2 generated 67 × 81 × 60 grid cells. A covariance value of 0.3 was uniformly applied in all directions for both models. Ultimately, a subset of 45 MT measurements was used, with 25 on Line 1 and 20 on Line 2.

For Line 1, the normalized root-mean-square (nR.M.S.) misfit of the inversion model decreased from 6.662 to 1.677 over 105 iterations,

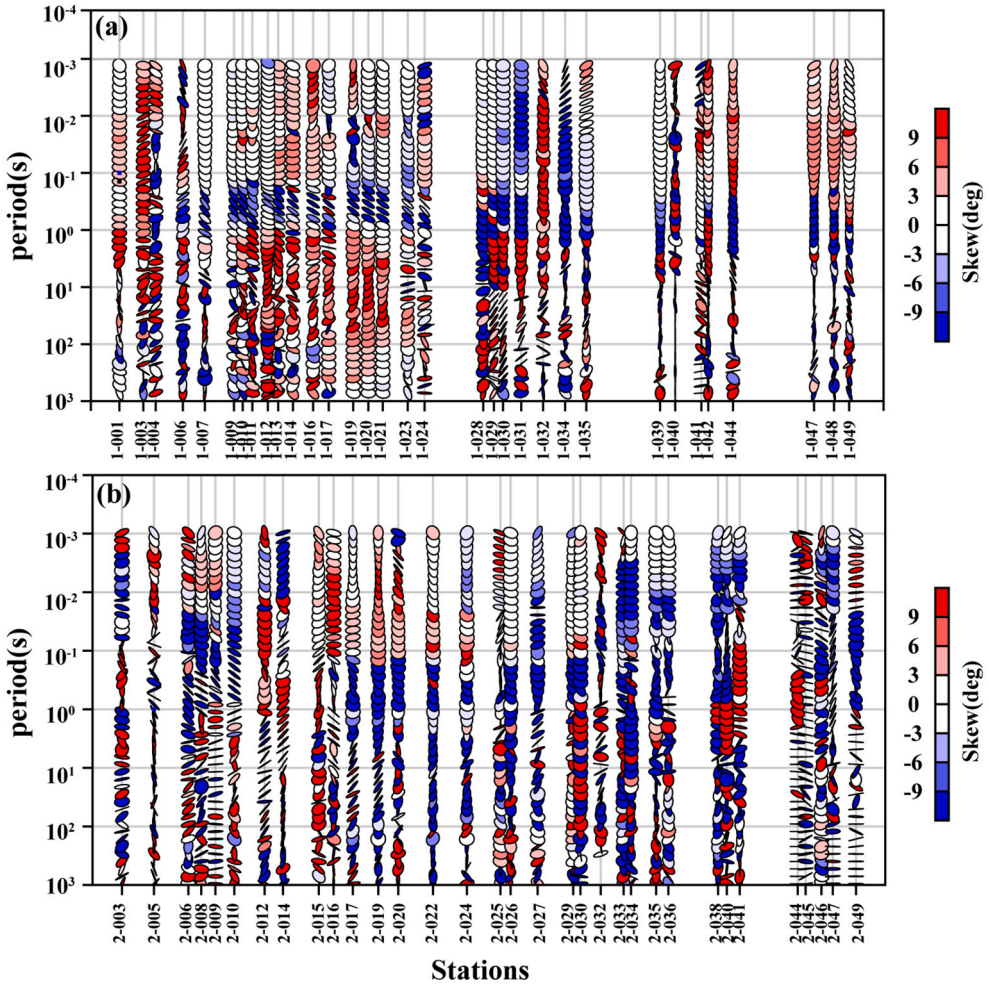


**Fig. 3.** Normalized phase tensor pseudo section along the MT lines with the right side pointing southeastward. (a) Line 1; (b) Line 2.

while that of Line 2 decreased from 7.211 to 1.854 after 107 iterations. These results indicate that the final models provide a good fit for the field data. Detailed comparisons between measured and modeled data further confirm that the models accurately reflect both the off-diagonal and diagonal components of the impedance tensor (Fig. 5 for the data fit of representative MT sites).

## 4. Results

Understanding the spatial distribution of electrical features in the study area is of great guiding significance for gaining insights into the geological structures associated with W-Sn mineralization in southern Hunan. The 3-D resistivity models (see Fig. 6 and Fig. 7) provide a detailed view of the upper crust of this area, revealing a heterogeneity and highlighting several notable features. For clarity, resistive features are labeled 'R', conductive features as 'C', and specific conductive structures related to the fault zones are labeled 'F' in the following description.

### *4.1. Line 1*

The vertical section along Line 1 reveals a subsurface medium primarily characterized by high resistivity. The section is divided into two sectors by a conductive zone consisting of conductors C14 and C15 (< 100 Ω·m). The western region beyond the conductive zone exhibits a distinct high-resistivity background, mainly consisting of high-resistivity structures marked R11 and R12 (> 500 Ω·m). Within this area, a series of discontinuous conductive structures (C11-C13; ~ 30 Ω·m) are distributed. This region corresponds to the Late Paleozoic strata encompassing the Qitianling pluton, which includes Devonian, Carboniferous, Permian and others. In contrast, the electrical structures to the east of the conductive zone appear simpler, featuring just one prominent high-resistivity feature, labeled R13 (> 1000 Ω·m). This structure extends vertically to a depth of approximately 5 km and corresponds to the position of the Qitianling pluton emerging at the southern margin with a well-defined lower interface.

According to available geological data, the conductor designated C11 (< 50 Ω·m) near the surface corresponds to the identified fault F1. However, limited MT data make it challenging to determine its spatial distribution within the geological strata. Conductor C12 (< 50 Ω·m) is composed of multiple conductive blocks with indistinct shapes, distributed within near-surface (< 4 km) strata, extending horizontally for ~ 7 km along Line 1. Surface faults labeled F2 and F3 align with this area. Conductor C13 (< 50 Ω·m) is situated southeast of C12 at a greater depth (> 4 km) and corresponds to Devonian and Carboniferous strata. The high-conductivity structure C14 (< 30 Ω·m) is flanked by resistive structures R12 and R13, and extends from the surface to ~ 5 km depth. It slopes towards the southeast (with an inclination angle of approximately 30°). The faults F4, F5, F6, and F7 identified near the surface as depicted in Fig. 6, likely control the spatial distribution of a series of W, Sn, and Pb-Zn deposits.

Directly below, the notable high-conductivity structure C15 (< 30 Ω·m) appears as a block within the 3–10 km depth range, extending horizontally over approximately 5 km. Furthermore, the conductive

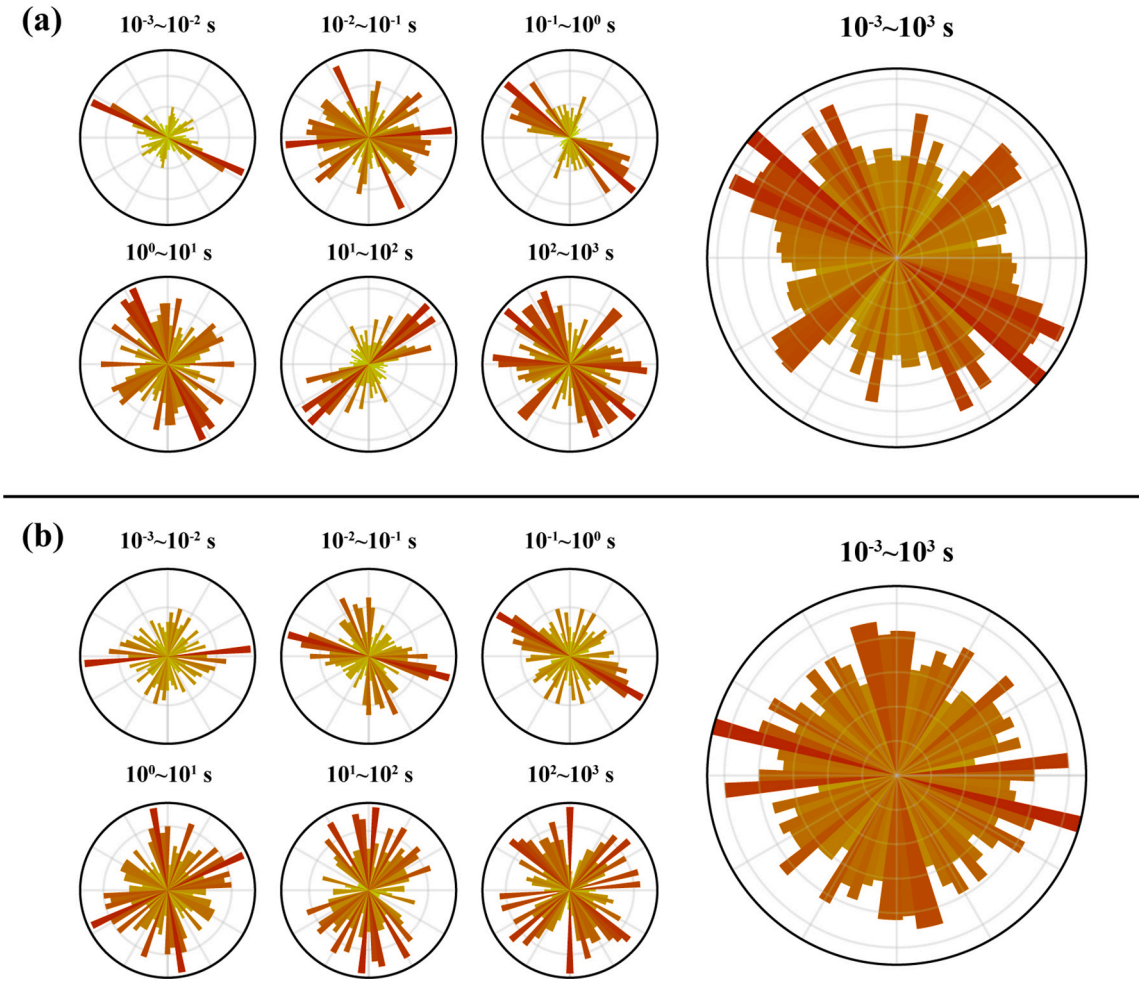


**Fig. 4.** Strike analysis results from the G-B decomposition at six-period bands ($10^{-3} \sim 10^{-2}$ s, $10^{-2} \sim 10^{-1}$ s, $10^{-1} \sim 10^{0}$ s, $10^{0} \sim 10^{1}$ s, $10^{1} \sim 10^{2}$ s and $10^{2} \sim 10^{3}$ s). (a) Line 1; (b) Line 2. Plotting was carried out using MTPy (Krieger and Peacock, 2014).

zone formed by C14 and C15 is distributed along the northwest flank of the high-resistivity structure R13. This zone represents a southeast-dipping normal fault (with an inclination angle of approximately 30°), extending downward to depths below 10 km in the upper crust. Geologically, this zone correlates to the (upper-) crustal scale Chenzhou-Linwu fault (CLF) system.

The high-resistivity region R11 extends from the surface downward to the deep strata along the southwest direction. In shallow strata (< 4 km), R11 encircles the conductive zone C12, while in the deeper strata (> 4 km), it primarily exhibits high-resistivity characteristics. The resistive area R12 extends nearly vertically from a depth of 1 km to 12 km. The resistive structure, along with the eastern section of R11, encloses conductor C13. R13, the most prominent high-resistivity structure in the eastern survey area, is characterized by a well-defined electrical boundary. It extends approximately 18 km along the profile, with a maximum vertical depth of ~ 5 km, corresponding to the exposed area of the Qitianling pluton at the surface.

### 4.2. Line 2

The vertical section along Line 2, running parallel to Line 1, reveals relatively distinct subsurface electrical resistivity boundaries (Fig. 7), as evidenced by block-like features. Similar to Line 1, the shallow zones of Line 2 exhibit high resistivities, as shown by areas marked as R22 and R23 (> 1000 Ω·m). This is accompanied by dispersed conductive structures C21, C22, and C24 (< 30 Ω·m). In contrast, the deeper strata are dominated by a single high-conductivity structure, labeled C23 (< 30 Ω·m), set against an inconspicuous middle-low resistivity background.

Descriptively, the conductive area C21 is situated at a depth of 1.5 km and extends horizontally along the profile for about 2 km. Its conductivity gradually decreases with depth, corresponding to the location of the Ping-Bao polymetallic ore deposits near the surface. The high-conductivity structure C22 is located between the resistive zones R21 and R22 and extends to depths of ~ 4–5 km. Near the surface, it correlates with fault F4, and its lower portion, descending below 1 km, slopes towards the southeast (with an inclination angle of approximately 40°). As the predominant high-conductivity structure, C23 appears as a distinct elongated-block-shape within the subsurface range of 3 km to 12 km. Its orientation is inclined towards the west. Above this conductor, there are known W and Pb-Zn deposits marked as Fig. 7, and its vertical projection onto the surface corresponds to the location of fault F5. And the conductive zone C24 lies to the southeast of R23 and is composed of multiple discontinuous small-scale conductive blocks (< 10 Ω·m), inclined overall towards the southeast.

The high-resistivity structure, R21 is located in the western sector of the survey. Its upper segment (< 2 km) has a high resistivity exceeding 1,000 Ω·m, and the lower portion has a relatively lower resistivity range of 300 Ω·m to 1000 Ω·m, extending downward to approximately 8 km and spanning a width of ~ 6 km. The high-resistivity structure R22 is positioned northwest of C23, with scattered occurrences of small-scale electrically weak zones. Within a vertical depth of 5 km, the horizontal distribution of R22 decreases as its downward extension increases. Located southeast of C23, the high-resistivity structure R23 aligns

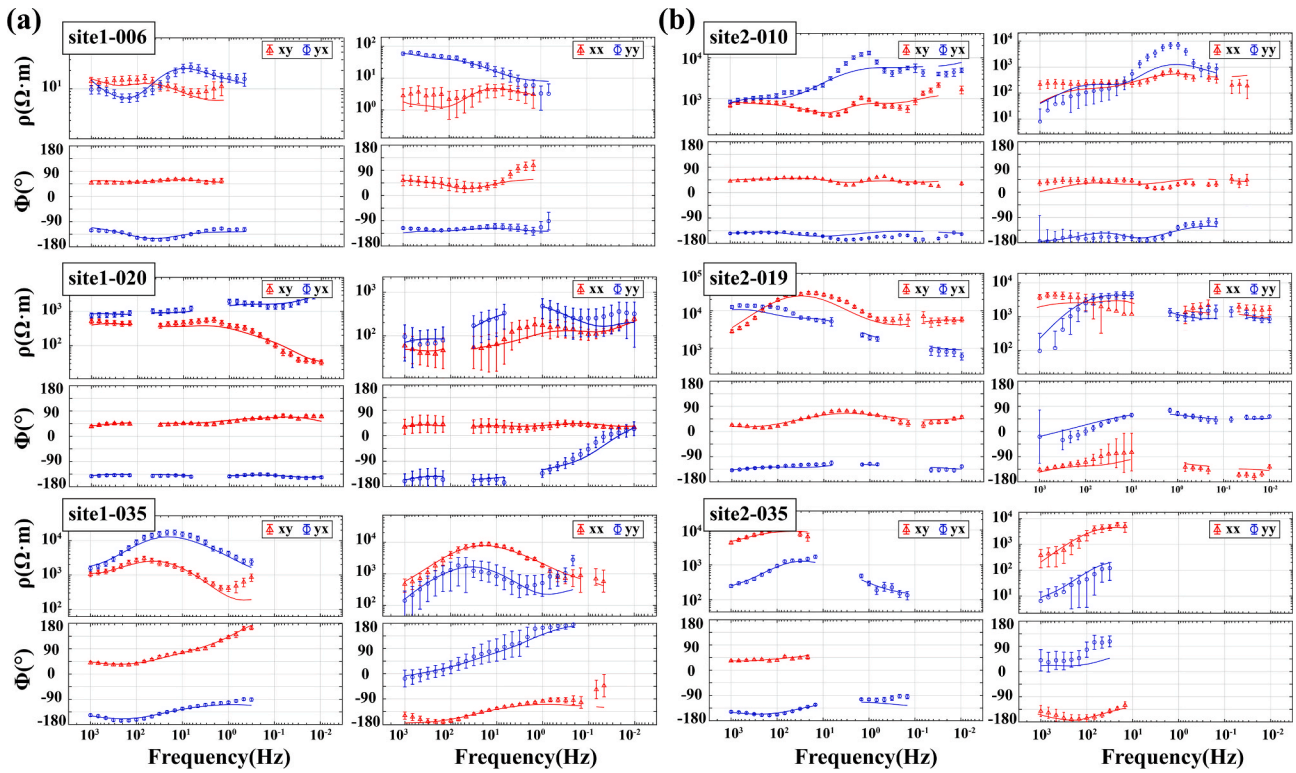


**Fig. 5.** The data fit of representative sites. (a) Line 1, including site 1–006, site 1–020, and site 1–035; (b) Line2, including site 2–010, site 2–019, and site 2–035.

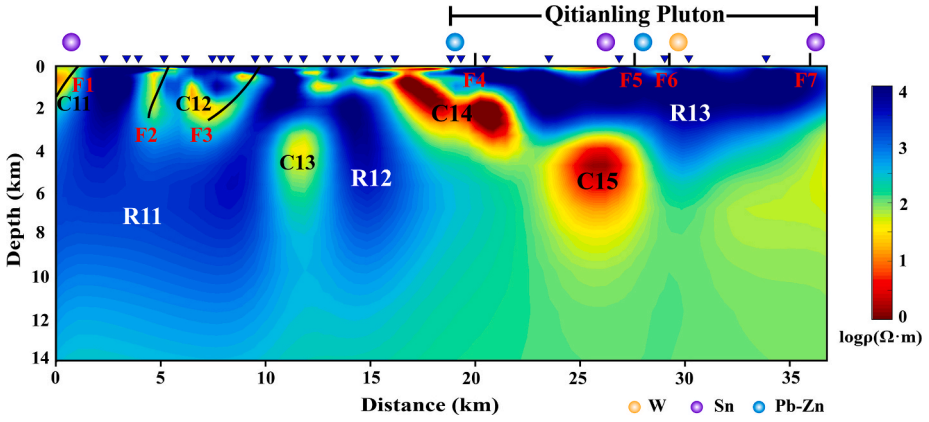


**Fig. 6.** NW-SE trending vertical slice of the 3-D inversion model along Line 1. Black solid lines numbered "F1" ~ "F7" are the main faults within southern Hunan, and colored circles indicated the location of deposits.

geometrically with R22, together constituting the primary part of the Qitianling pluton.

## 5. Discussion

The preliminary spatial distribution characteristics of the electrical structures in the Qitianling region of southern Hunan have been derived based on Fig. 8. Subsequently, we will interpret the geophysical results using geological, geochemical, and other geophysical data to discuss the geological structural significance of key electrical features. Moreover, supported by previous studies, we will further discuss the spatial emplacement model of the Qitianling pluton.

### *5.1. The migration paths of magma hydrothermal fluids*

According to existing geological data (cf., Shen Hongfei, 2022), faults labeled as F1-F8 (Fig. 8) are associated with the crustal-scale Chenzhou-Linwu northeast-trending fault system. This fault system serves as a conduit for a substantial upwelling of magmatic-hydrothermal fluid carrying ore-forming materials and heat from the lower crust and even the upper mantle (cf. Boukhalfa et al., 2024; Yu et al., 2022), thereby facilitating the emplacement of diverse polymetallic ore deposits, such as the Baoshan Pb-Zn deposit, the Huangshaping W-Mo-Cu deposit, the Xintianling W-Mo deposit, and the Furong Sn deposit (Mao et al., 2021; Chen et al., 2021; Yuan et al., 2019). Moreover, the fault system plays a crucial role in guiding the spatial emplacement of large-scale deposits and massive granitic intrusions associated with Qitianling pluton.

The research of Tang et al. (2015, 2023) indicated that neutral buoyancy is attained when medium-acidic magmas sourced from the deep lithospheric mantle intrude into the upper crust to a depth of about 5 km, leading to the formation of terminal magma reservoirs and related

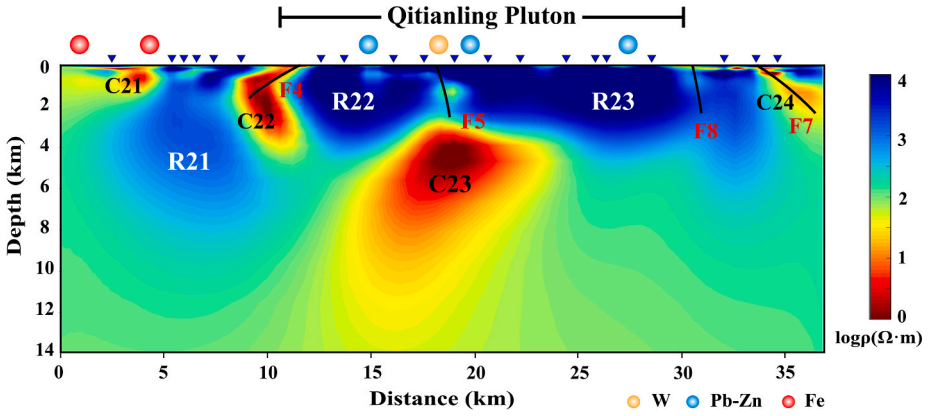


**Fig. 7.** NW-SE trending vertical slice of the 3-D inversion model along Line 2. Black solid lines numbered "F4", "F5", "F7", "F8" are the main faults within southern Hunan, and colored circles indicated the location of deposits.

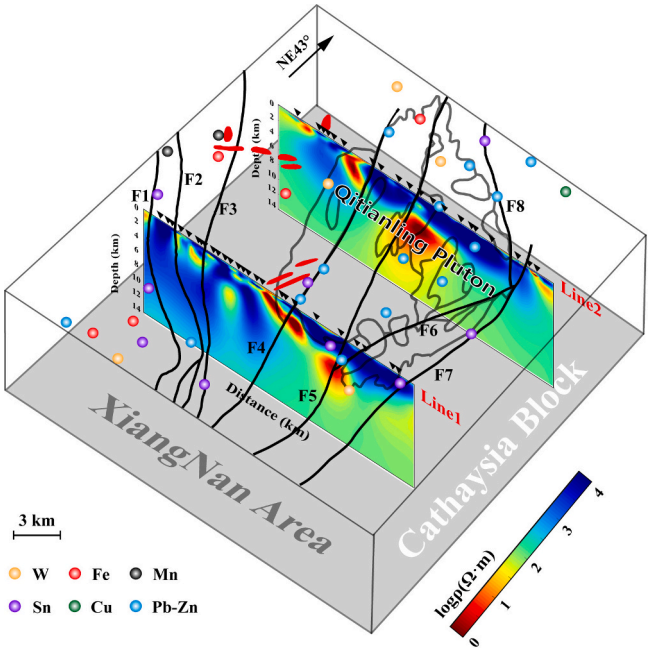


**Fig. 8.** Three-dimensional resistivity models generated from MT data shown along two lines. The overlay shows the main faults (black lines), mineral deposits (colored spheres), lamprophyre dykes (red zones), and the outline of the Qitianling pluton complex from surface geology (gray lines), as in Fig. 1.

host rock alteration. Within this region, substantial deposition of sulfide minerals through pre-enrichment processes gives rise to pronounced high-conductivity features (e.g., Comeau et al., 2024; Comeau et al., 2022; Yin et al., 2021). Based on this finding, it is reasonable to suggest that the electrical structures C15 and C23 (see Fig. 6 and Fig. 7, respectively), which developed beneath the Qitianling pluton, likely represent magma and melt reservoirs where continuing fractional crystallization and assimilation mingling occurred before magma and fluid emplacement into the shallow crust (< 3 km), after ascending from the deep lithosphere.

Given the regional geological background, the genesis of conductive structures within shallow strata is intricate, with primary manifestations including expressions of rock weathering, lithological alteration/fracture zones, structural fault systems, as well as Quaternary sediments. According to Fig. 8, small-scale regional faults (F1-F4) are mainly situated on the northwest flank of the Qitianling pluton, serving as conduits facilitating the migration of ore-forming materials and energy for polymetallic deposits (cf., Yu et al., 2022; Mao et al., 2021). In addition, the secondary small-scale faults and fractures derived from them provided favorable spaces for the precipitation and enrichment of ore-forming fluids, thereby controlling the morphology and occurrence of ore bodies (cf., Shen Hongfei, 2022; He et al., 2016). Therefore, within the polymetallic ore fields centered around the Qitianling pluton (apart from the Xianghualing Sn ore bodies, which mostly occur at the unconformable interfaces between the Cambrian epimetamorphic rocks series and the upper Devonian clastic rocks series), most are primarily hosted within the Late Paleozoic Devonian-Carboniferous strata. Moreover, their morphology and occurrence are governed by the NNE-NE trending structures and their associated secondary structural systems.

### 5.2. *Upper-crustal resistive structures and their geological significance*

The research area is divided into two distinct sectors, based on the observed electrical resistivity, with the separation being the fault zone F4, as depicted in Fig. 8. The high-resistivity features (R13, R22, and R23) to the east are closely correlated with the Qitianling granitic pluton. The electrical resistivity model appears to indicate that the Qitianling pluton is rootless with a buried depth of about 5 km, which aligns with the geometric characteristics proposed by Liu et al. (2018) based on gravity modeling. Additionally, a velocity model derived from a synthetic seismic profile traversing the Qitianling pluton unveiled a conspicuous low-velocity anomaly (< 5800 m/s) in the shape of a funnel that appeared in the upper 5–10 km (Fig. 9c, modified from Li et al., 2014), corresponding well with the morphology depicted in the electrical resistivity models (Fig. 9a and Fig. 9b). This is in contrast to the inferred result of a flat bottom based on gravity modeling as shown in Liu et al. (2018). These findings provide additional validation for the reliability of the inferred burial morphology of the pluton based on the 3-D electrical resistivity models, whereas the outline of the low Bouguer gravity anomaly denotes very clearly the lateral extent of the pluton (Fig. 10).

On the other hand, the Late Paleozoic strata, comprising the Permian, Carboniferous, and Devonian, as illustrated in Fig. 1, primarily consist of carbonate rocks, such as dolomite, dolomitic limestone, and limestone, corresponding to high-resistivity structures (R11, R12, and R21) situated to the west of fault F4 in the electrical resistivity models. Rock physical property tests of the southern Hunan region conducted by Shen Hongfei (2022) suggested that dolomite and dolomitic limestone rocks exhibit significantly high resistivity, with a mean value exceeding 10,000 Ω·m, whereas the resistivity of limestone is somewhat lower, typically ranging between 3,000 Ω·m and 5,000 Ω·m. Fractured and argillaceous limestones demonstrate lower resistivity still, attributed to their high porosity and aquosity, with a mean resistivity of ~ 2,000 Ω·m. Carbonaceous limestone, sandstone, and mudstone typically display resistivity values below 1,000 Ω·m. Within these resistive formations,

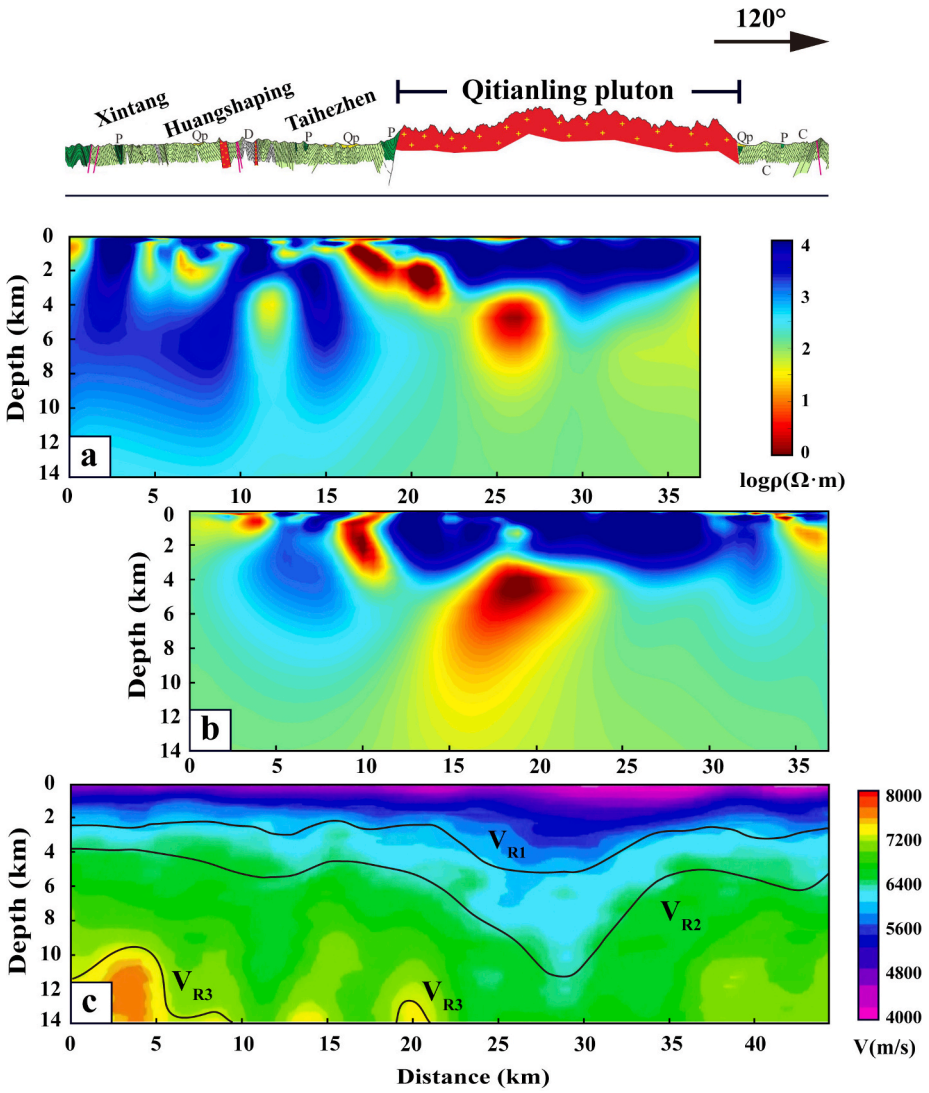


**Fig. 9.** Comparison between electrical resistivity models and seismic velocity model within southern Hunan. (a) image the vertical slice of the inversion model along Line 1, and (b) for that along Line 2; (c) The velocity model created from the inversion of reflected seismic waves, modified from Li et al. (2014), with the black solid lines depict the velocity isolines labeled $V_{R1}$, $V_{R2}$ and $V_{R3}$. In addition, the upper panel shows the regional geology and the Qitianling pluton.

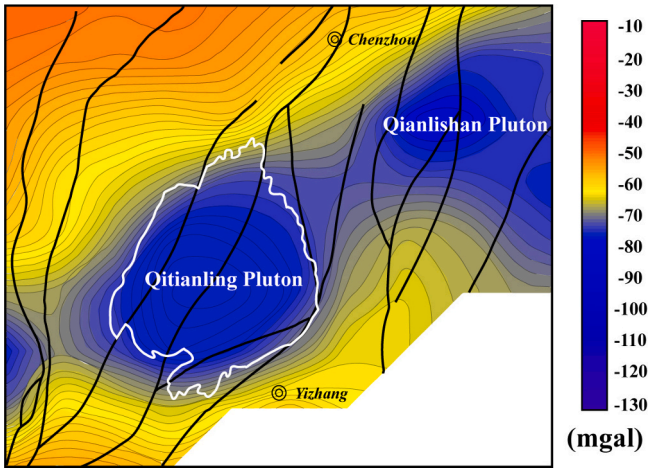


**Fig. 10.** Residual Bouguer gravity anomaly map related to the Qitianling pluton and its surrounding region, proposed by Geological Bureau of Hunan Province (2013). The black solid lines represent the main faults, and the white solid line outlines the Qitianling pluton.

electrically conductive zones (e.g., C12 and C13 in Fig. 6) appear as medium–low resistivity features, suggesting a probable association with lithological alteration/fracture zones or the presence of (coal-bearing) clastic rocks.

### 5.3. *Emplacement model of the Qitianling pluton*

Understanding the spatial emplacement mechanism of the most representative granite pluton in Southern Hunan is significant for elucidating the systems of the fluid- and ore-controlling structures and regional metallogenic prediction. Therefore, from the perspective of deep electrical resistivity features, we discuss the possibility of a more thorough emplacement mechanism for the Qitianling pluton, and made the conceptual cartoon of the intrusion model of the Qitianling pluton (Fig. 11).

The Qitianling pluton is a multi-stage complex batholith formed during the early Yanshanian orogeny and can be divided into three distinct intrusion stages (cf., Shen Hongfei, 2022; Liu et al., 2018; He et al., 2016; Li et al., 2014; Zhu et al., 2009). Phase I (160 ~ 163 Ma): This phase involves the low-density melt resulting from partial melting of the Precambrian crystalline basement intruded along major deep-seated faults driven by regional tectonic activities (He et al., 2016).

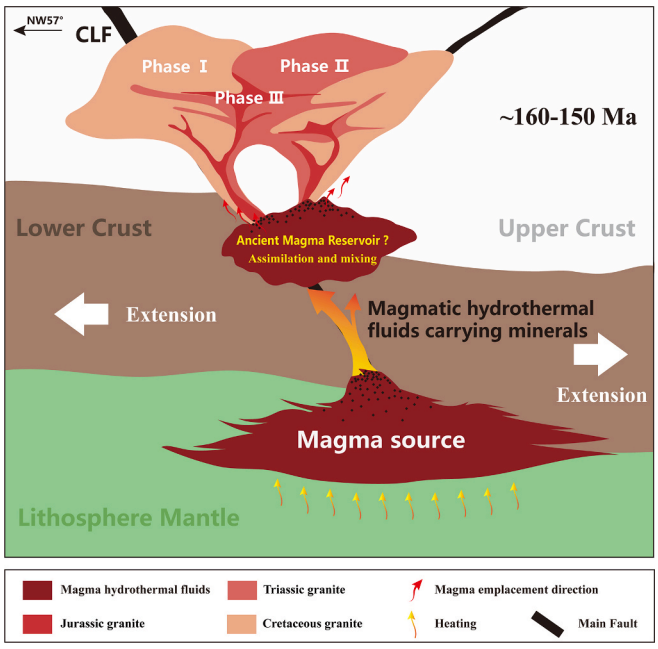


**Fig. 11.** Conceptual cartoon of the intrusion model of the Qitianling pluton. The small black dots denote mineral particles within the magma, which can be transported to the upper crust by magmatic-hydrothermal fluid migration (cf., Tang et al., 2023; Li et al., 2018).

Following that, the magma underwent cooling and solidification in the near-surface strata, initiating the formation of Phase I granite. This granite predominantly occurred along the eastern, northern, and western margins of the intrusion, and consists of amphibole- and biotite-bearing granite with locally abundant mafic enclaves and K-feldspar megacrysts (Liu et al., 2018; Chen et al, 2021). Emplacement during this phase was primarily controlled by deep-seated faults. The magma and mineralogical constituents mainly result from partial melting of the Precambrian crystalline basement, potentially accompanied by limited assimilation and hybridization of mantle-derived materials (Zhao et al., 2023). This phase also featured widespread intrusions with relatively subdued mineralization (cf., He et al., 2016; Li et al., 2021).

Phase II (153 ~ 157 Ma): During this phase, the regional magmatic-tectonic interactions, caused the closure of the deep-seated crustal faults due to tectonic stress, thereby subjecting the intruding magma to substantial pressure from surrounding rocks. This dynamic environment promotes the rapid ascent of magma along faulted conduits and into upper-crust faults, resulting in the formation of magma reservoirs (cf., Tang et al., 2023). Subsequently, propelled by dynamic and thermal energy from deep hydrothermal fluids, magma intruded into the structural weak zones between the phase I granite and the surrounding rocks or the associated secondary faulted systems, solidifying upon cooling to establish the initial state of Phase II granite. Phase II granite partially overlays Phase I granite, mainly distributed in the central and southern sectors of the Qitianling pluton (Liu et al., 2018). The predominant lithology formed in this stage is biotite granite. Unlike the first stage, magma emplacement during this stage was controlled not only by deep crustal faults but also by the spatial position of Phase I granite. As shallow magma cooled and solidified, the morphology of the Qitianling intrusive body developed.

Phase III (146 ~ 150 Ma): Driven by deep magma dynamics and country rock stress, magmatic-hydrothermal fluids ascended in batches along the structural weak zones between Phase I and Phase II granites. These fluids are predominantly emplaced in the form of stocks and dikes within structural fracture zones and/or joint fissures (cf., Li et al., 2021). Phase III granites, which are mostly characterized by fine-grained (or porphyritic) biotite granite, are essentially distributed in the southern portion of the Qitianling pluton. This stage was mainly influenced by the spatial distribution of granites from the preceding stages. According to the theory of "small intrusive mineralization" proposed by Tang et al. (2023), it is hypothesized that as residual ore-bearing magma precipitates and accumulates within the terminal magma reservoir, there is an enormous potential for the development of large-scale, high-grade concealed ore bodies at the high- and low-resistivity transition zones ranging from −2 km to −6 km within the Qitianling pluton.

Field and microscopic observations conducted by Liu et al. (2018) indicated that the composition and minerals of granites evolve continuously from Phase I to Phase III. On the other hand, the diagenetic and metallogenic ages within the research area were concentrated between 160 Ma and 150 Ma, encompassing intervals of tectonic inactivity between distinct stages (Yuan et al., 2019; Chen et al., 2022). This indicates that the magmatic emplacements in the Qitianling area were a continuous process. During these tectonic inactivity periods, deep thermal sources were supplied to shallow magma reservoirs through deep-seated faults, maintaining continuous assimilation and mingling between magma and strata (cf., Comeau et al., 2022). Additionally, Chen et al. (2022) revealed that cassiterite minerals associated with the skarn-type, chlorite-type, greisen-type, and quartz vein-type mineralizations in the Furong tin deposits all originated from the same magma-hydrothermal system. This finding supports the hypothesis that the conductive structures C15 and C23 represent the terminal magma reservoir, serving as sites where extensive fluid-rock interaction and element exchange took place between ore-bearing magma and surrounding rocks before emplacement.

## 6. Conclusions

Magnetotelluric data collected from an array of two long lines spanning the Qitianling pluton and its surrounding area in southern Hunan, which host a variety of tungsten- and tin-related deposits. The data were inverted to produce 3-D electrical resistivity models extending to depths of approximately 10 km. The model reveals a pronounced high-resistivity (> 1000 Ω·m; R13 and R22-R23) consistent with the location of the Qitianling pluton, thus clearly delineating its subsurface geometric features. Thin conductive structures (< 30 Ω·m; C14 and C22) appearing at the sides of the pluton are inferred to be crustal-scale fault systems. These are hypothesized to have provided favorable channels for the migration of ore-bearing fluids and energy accumulation. Broad conductive zones (< 30 Ω·m; C15 and C23) below the inferred pluton likely indicate the terminal magma reservoir where substantial fluid-rock interactions and element exchanges occurred prior to emplacement. Building upon these insights, we have proposed a multi-stage magmatic emplacement model for the Qitianling pluton. This model is primarily influenced by the spatial distribution of the regional fault system, surrounding rocks (predominately composed of limestone), and the pre-existing granites. Ultimately this gives new insights into the development of the W-Sn polymetallic mineralization system and the regional magmatic evolution.

## Funding sources

This work was supported by the 2022 Key project of the National Natural Science Foundation of China [grant number 42130810]; the Graduate Research Innovation Project of Central South University (Independent Exploration) [grant number 512340003]; and the Research project of Hunan Geological Institute [grant numbers HNGSTP 2022012023JJ60164].

## Declaration of competing interest

The authors declare that they have no known competing financial interests or personal relationships that could have appeared to influence the work reported in this paper.

## Acknowledgements

We thank Gary Egbert, Anna Kelbert, Naser Meqbel, and colleagues for sharing the 3-D inversion code MODEM. We thank Gary NcNeice and Alan Jones for sharing the tensor decomposition codes. We thank Jiankang Li of Insititute of Mineral Resources, CAGS for the seismic model. We thank Rujun Chen for the data acquisition instruments. We thank all the faculty and graduate students of the electromagnetic group at Central South University for providing supports for MT data collection and processing.

## Data availability

Data will be made available on request.

## References

Booker, J.R., 2014. The magnetotelluric phase tensor: a critical review. Surv. Geophys. 35 (1), 7–40.
Boukhalfa, Z., Benhallou, A.Z., Comeau, M.J., Bouzid, A., Bendaoud, A., Deramchi, A., 2024. The structure of a continental intraplate volcanic system and controls from shear zones: insights into the central Hoggar Cenozoic volcanic province, Northwest Africa, from electrical resistivity images. Gondw. Res. 135, 133–150.
Cagniard, L., 1953. Basic theory of the magneto-telluric method of geophysical prospecting. Geophysics 18, 605–635.
Caldwell, T.G., Bibby, H.M., Brown, C., 2004. The magnetotelluric phase tensor. Geophys. J. Int. 158 (2), 457–469.
Cawood, P.A., Wang, Y.J., Xu, Y.J., Zhao, G.C., 2013. Locating South China in Rodinia and Gondwana: a fragment of greater India lithosphere? Geology 41 (08), 903–906.
Chave, A.D., Jones, A.G., Mackie, R., Rodi, W., 2012. The Magnetotelluric Method: Theory and Practice. Cambridge University Press, Cambridge.
Chen, G.X., Liu, T.Y., Sun, J.S., Cheng, Q.M., Sahoo, B., Zhang, Z.J., Zhang, H.L., 2015. Gravity method for investigating the geological structures associated with W–Sn polymetallic deposits in the Nanling Range, China. J. Appl. Geophys. 120, 14–25.
Chen, S.C., Yu, J.J., Bi, M.F., 2021. Extraction of fractionated interstitial melt from a crystal mush system generating the Late Jurassic high-silica granites from the Qitianling composite pluton, South China: implications for greisen-type tin mineralization. Lithos 382, 105952.
Chen, S.C., Yu, J.J., Bi, M.F., Li, H.M., Lehmann, B., 2022. Cassiterite U–Pb, mica 40Ar–39Ar dating and cassiterite trace-element composition of the Furong tin deposit in the Nanling Range, South China. Ore Geol. Rev. 143, 104775.
Cheng, Y., Spandler, C., Chang, Z., Clarke, G., 2018. Volcanic-plutonic connections and metal fertility of highly evolved magma systems: a case study from the Herberton Sn-W-Mo mineral field, Queensland, Australia. Earth Planet. Sci. Lett. 486, 84–93.
Comeau, M.J., Becken, M., Kuvshinov, A.V., 2022. Imaging the whole-lithosphere architecture of a mineral system—geophysical signatures of the sources and pathways of ore-forming fluids. Geochem. Geophys. Geosyst. 23 (08).
Comeau, M.J., Becken, M., Kuvshinov, A.V., Demberel, S., 2021. Crustal architecture of a metallogenic belt and ophiolite belt: Implications for mineral genesis and emplacement from 3-D electrical resistivity models (Bayankhongor area, Mongolia). Earth Planets Space 73 (01), 82.
Comeau, M.J., Rigaud, R., Batmagnai, E., Tserendug, S., Kuvshinov, A., Becken, M., Demberel, S., 2024. Insights into the structure of the Mongol-Okhotsk Suture Zone, Adaatsag ophiolite, and tectonic boundaries of the central asian orogenic belt (mongolia) from electrical resistivity imaging and seismic velocity models. J. Geophys. Res. Solid Earth 129 (04) e2023JB028503.
Dai, Q.W., Duan, D., Liu, B., Wu, Q.H., Yan, J.B., Kong, H., Chen, S.F., Zong, Q., Tang, Y. Y., 2023. Deep exploration of W−Sn and Cu polymetallic deposits in middle Qin−Hang metallogenic belt, South China. Trans. Nonferrous Met. Soc. Chin. 33 (01), 231–253.
Dentith, M., Yuan, H., Johnson, S., Murdie, R., Piña-Varas, P., 2018. Application of deep-penetrating geophysical methods to mineral exploration: Examples from Western Australia. Geophysics 83 (3). WC29–WC41.
Egbert, G.D., Kelbert, A., 2012. Computational recipes for electromagnetic inverse problems. Geophys. J. Int. 189, 251–267.
Faure, M., Lin, W., Chu, Y., Lepvrier, C., 2016. Triassic tectonics of the southern margin of the South China Block. C. R. Geosci. 348 (1), 5–14.
Faure, M., Lepvrier, C., Nguyen, V.V., Vu, T.V., Lin, W., Chen, Z.C., 2014. The South China block-Indochina collision: where, when, and how? J. Asian Earth Sci. 79, 260–274.
Gamble, T.D., Goubau, W.M., Clarke, J., 1979. Magnetotellurics with a remote magnetic reference. Geophysics 44, 53–68.
Groom, R.W., Bailey, R.C., 1989. Decomposition of magnetotelluric impedance tensors in the presence of local three-dimensional galvanic distortion. J. Geophys. Res. Solid Earth 94, 1913–1925.
Guo, Z.W., Xue, G.Q., Liu, J.X., Wu, X., 2020. Electromagnetic methods for mineral exploration in China: a review. Ore Geol. Rev. 118, 103357.
He, H.H., Wang, D.K., Su, X.Y., Zhang, Y.J., Wang, G.R., Li, J.K., Zhao, B., Li, J.G., 2014. Geochemical Characteristics and ore potential of rare metal elements of the qitianlin batholith in South Hunan, China. Geotect. Metallogenia 38 (02), 366–374.
He, H.H., Wang, D.K., Wang, R.J., Li, J.K., Zhao, Z., Huang, F., Yu, Y., Zhang, Y.J., 2016. Metallogenic characteristics comparison between Qitianling and Xianghualing intrusion in South Hunan. J. Guilin Univ. Technol. 36 (01), 76–89.
Heinson, G., Didana, Y., Soeffky, P., Thiel, S., Wise, T., 2018. The crustal geophysical signature of a world-class magmatic mineral system. Sci. Rep. 8 (1), 10608.
Hill, G.J., Bibby, H.M., Ogawa, Y., Wallin, E.L., Bennie, S.L., Caldwell, T.G., Keys, H., Bertrand, E.A., Heise, W., 2015. Structure of the Tongariro Volcanic system: Insights from magnetotelluric imaging. Earth Planet. Sci. Lett. 432, 115–125.
Hu, R.Z., Chen, W.T., Xu, D.R., Zhou, M.F., 2017. Reviews and new metallogenic models of mineral deposits in South China: An introduction. J. Asian Earth Sci. 137, 1–8.
Huang, F.F., Scaillet, B., Wang, R.C., Erdmann, S., Chen, Y., Faure, M., Liu, H.S., Xie, L., Wang, B., Zhu, J.C., 2019. Experimental constraints on intensive crystallization parameters and fractionation in A-Type granites: a case study on the Qitianling Pluton, South China. J. Geophys. Res. Solid Earth 124 (10), 10132–10152.
Jin, S., Sheng, Y., Comeau, M.J., Becken, M., Wei, W.B., Ye, G.F., Dong, H., Zhang, L.T., 2022. Relationship of the crustal structure, rheology, and tectonic dynamics beneath the Lhasa-Gangdese Terrane (Southern Tibet) based on a 3-D electrical model. J. Geophys. Res. Solid Earth 127 (01), e2022JB024318.
Kelbert, A., Meqbel, N., Egbert, G.D., Tandon, K., 2014. ModEM: A modular system for inversion of electromagnetic geophysical data. Comput. Geosci. 66, 40–53.
Krieger, L., Peacock, J.R., 2014. MTpy: a Python toolbox for magnetotellurics. Comput. Geosci. 72, 167–175.
Li, H., Palinkas, L., Watanabe, K., Xi, X.S., 2018. Petrogenesis of Jurassic A-type granites associated with Cu-Mo and W-Sn depositsin the central Nanlingregion, South China: Relation to mantle upwelling and intra-continental extension. Ore Geol. Rev. 92, 449–462.
Li, H.M., Li, L.X., Yu, J.J., Ma, S.X., Li, X.S., Shen, H.F., 2021. Mineral assemblages, mineralized alteration and ore-forming fluid composition of the W-Sn polymetallic deposits of South Hunan. Acta Geol. Sin. 95 (10), 3127–3145.
Li, J.G., Li, J.K., Wang, D.H., Liu, J., He, H.H., 2014. The deep tectonic features of Qitianling ore-concentrated area in southern Hunan Province and its contrains to the regional ore-forming process. Acta Geol. Sin. 88 (04), 695–703.
Liu, H.S., Martelet, G., Wang, B., Erdmann, S., Chen, Y., Faure, M., Huang, F.F., Scaillet, B., Le-Breton, N., Shu, L.S., Wang, R.C., Zhu, J.C., 2018. Incremental emplacement of the Late Jurassic Midcrustal, Lopolith-Like Qitianling Pluton, South China, revealed by AMS and Bouguer Gravity Data. J. Geophys. Res. Solid Earth 123 (10), 9249–9268.
Liu, J.X., Zhou, K.K., Liu, H.D., Guo, R.W., Zhu, Y.Q., Zhang, Z.H., Liu, R., 2023. Metallogenic prediction of magnetite in the pandian area at the Northwest Margin of Luxi Uplift, China: constraints of wide-field electromagnetic data. Remote Sens. (Basel) 15 (05), 1217.
Lü, Q., Meng, G., Zhang, K., Liu, Z., Yan, J., Shia, D., et al., 2021. The lithospheric architecture of the lower Yangtze metallogenic Belt, East China: insights into an extensive Fe–Cu mineral system. Ore Geol. Rev. 132, 103989.
Mao, J.W., Cheng, Y.B., Chen, M.H., Franco, P., 2013. Major types and time-space distribution of Mesozoic ore deposits in South China and their geodynamic settings. Miner. Deposita 48, 267–294.
Mao, J.W., Xie, G.Q., Yuan, S.D., Liu, P., Meng, X.Y., Zhou, Z.H., Zheng, W., 2018. Current research progress and future trends of porphyry-skarn copper and granite-related tin polymetallic deposits in the Circum Pacific metallogenic belts. Acta Petrol. Sin. 34, 2501–2517.
Mao, X., Ye, G.F., Zhang, Y.X., Jin, S., Wei, W.B., 2021. Electrical structure of the southern section of the Jiangnan orogenic belt and its tectonic implications. Chin. J. Geophys. 64 (11), 4043–4059.
McNeice, G.W., Jones, A.G., 2001. Multisite, multifrequency tensor decomposition of magnetotelluric data. Geophysics 66 (1), 158–173.
Ni, P., Pan, J.Y., Han, L., Cui, J.M., Gao, Y., Fan, M.S., Li, W.S., Chi, Z., Zhang, K.H., Cheng, Z.L., Liu, Y.P., 2023. Tungsten and tin deposits in South China: Temporal and spatial distribution, metallogenic models and prospecting directions. Ore Geol. Rev. 157, 105453.
Qu, L.J., Wang, Q., Li, B., Yao, W., 2020. The application of multiple geophysical methods to the study of deep metallogenic regularity in the Sanhexu mining area, the Xianghualing orefield, Hunan Province. Geophys. Geochem. Expl. 44 (06), 1313–1321.
Schmidt, C., 2018. Formation of hydrothermal tin deposits: Raman spectroscopic evidence for an important role of aqueous Sn (IV) species. Geochim. Cosmochim. Acta 220, 499–511.
Shen, H.F., 2022. Main controlling factors of Mesozoic Tungsten-Tin Polymetallic Mineralization in South Hunan (Phd thesis). Chinese Academy of Geological Science.
Sheng, Y., Jin, S., Comeau, M.J., Becken, M., Zhang, L., Dong, H., et al., 2022. Controls on the metallogenesis of the Lhasa–Mozugongka district, Gangdese Belt, Tibetan Plateau: Constraints on melt distribution and viscosity from the 3-D electrical structure of the lithosphere. Ore Geol. Rev. 145, 104881.
Sheng, Y., Jin, S., et al., 2023. Evidence for partial melting and alkali-rich fluids in the crust from a 3-D electrical resistivity model in the vicinity of the Coqen region, western Lhasa terrane, Tibetan Plateau. Earth Planet. Sci. Lett. 619, 118316.
Sheng, Y., Jin, S., Comeau, M.J., Hou, Z., Yin, Y., Zhang, L., et al., 2024. Crustal conductivity footprint of the Miocene porphyry copper polymetallic deposits in the Gangdese metallogenic belt, Tibetan Plateau. Ore Geol. Rev. 168, 106033.
Shu, X.J., Wang, X.L., Sun, T., Xu, X.S., Dai, M.N., 2011. Trace elements, U–Pb ages and Hf isotopes of zircons from Mesozoic granites in the western Nanling Range, South China: implications for petrogenesis and W–Sn mineralization. Lithos 127 (3–4), 468–482.
Tang, Z.L., Jiao, J.G., Yan, H.Q., Xu, G., 2015. Theoretical system for (large) deposit formed by smaller intrusion. Strategic Study of CAE 17 (2), 4–18+2.

Tang, Z.L., Duan, J., Xu, G., Qian, Z.Z., Yan, H.Q., Jiao, J.G., Chen, Y.Y., 2023. Theory and practice of small intrusive mineralization. J. Earth Sci. Environ. 45 (05), 1015–1025.

Tikhonov, A., 1950. On determining electrical characteristics of the deep layers of the Earth's crust. Dokl. Acad. Nauk SSSR 73, 295–297.

Wang, Y.F., Guo, R.W., Liu, J.X., Li, J., Liu, R., Chen, H., et al., 2024. A divergence-free vector finite-element method for efficient 3D magnetotelluric forward modeling. Geophysics 89 (01), E1–E11.

Xie, L., Wang, R.C., Chen, J., Zhu, J.C., 2010. Mineralogical evidence for magmatic and hydrothermal processes in the Qitianling oxidized tin-bearing granite (Hunan, South China): EMP and (MC)-LA-ICPMS investigations of three types of titanite. Chem. Geol. 276, 53–68.

Xu, S., Hu, X.Y., Chen, C.J., Yang, X., Sun, H.P., 2023. The western segment of the precambrian suture between the Yangtze and Cathaysia Blocks: constraints from magnetotelluric data in southwest China. Geophys. Res. Lett. 50 (04) e2022GL101872.

Xu, S., Unsworth, M.J., Hu, X.Y., Mooney, W.D., 2019. Magnetotelluric evidence for asymmetric simple shear extension and lithospheric thinning in South China. J. Geophys. Res. Solid Earth 124 (01), 104–124.

Yin, Y.T., Jin, S., Wei, W.B., Lü, Q.T., Ye, G.F., Jing, J.E., Zhang, L.T., Dong, H., Xie, C.L., 2021. Lithosphere structure and its implications for the metallogenesis of the Nanling Range, South China: constraints from 3-D magnetotelluric imaging. Ore Geol. Rev. 131, 104064.

Yu, N., Wang, E.C., Wang, X.B., Kong, W.X., Li, D.W., Li, R.H., 2022. The influence of the Ailaoshan-Red River shear zone on the mineralization of the Beiya deposit on the southeastern margin of the Tibetan Plateau revealed by a 3-D magnetotelluric survey. J. Geophys. Res. Solid Earth 127 (02), e2021JB022923.

Yuan, L.L., Wang, Y.F., Liu, J.P., Shao, Y.J., Liu, Z.F., Li, B., Zheng, X., Ding, T., Zhang, T. D., 2022. Petro-geochemistry of Late Jurassic highly fractionated granites in the Xianghualing area of Hunan Province: constrains on petrogenesis and rare-metal mineralization. Acta Petrol. Sin. 38 (07), 2113–2138.

Yuan, S.D., Williams-Jones, A.E., Romer, R.L., Zhao, P.L., Mao, J.W., 2019. Protolith-related thermal controls on the decoupling of Sn and W in Sn-W metallogenic Provinces: Insights from the Nanling Region, China. Econ. Geol. 114 (5), 1005–1012.

Zhao, D., Han, R.S., Liu, F., Fu, Y.X., Zhang, X.P., Qiu, W.L., 2023. Research Progress of magmatic hydrothermal mineralization in the polymetallic ore concentration area of Southern Hunan. Geotecton. Metallog. 47 (02), 337–360.

Zhao, K.D., Jiang, S.Y., Yang, S.Y., Dai, B.Z., Lu, J.J., 2012. Mineral chemistry, trace elements and Sr-Nd-Hf isotope geochemistry and petrogenesis of Cailing and Furong granites and mafic enclaves from the Qitianling batholith in the Shi-Hang zone, South China. Gondwana Res. 22 (01), 310–324.

Zhao, K.D., Jiang, S.Y., Nakamura, E., Moriguti, T., Palmer, M.R., Yang, S.Y., Dai, B.Z., Jiang, Y.H., 2011. Fluid–rock interaction in the Qitianling granite and associated tin deposits, South China: evidence from boron and oxygen isotopes. Ore Geol. Rev. 43 (01), 243–248.

Zhu, J.C., Wang, R.C., Zhang, P.H., Xie, C.F., Zhang, W.L., Zhao, K.D., Xie, L., Yang, C., Che, X.D., Yu, A.P., Wang, L.B., 2009. Zircon U-Pb geochronological framework of Qitianling granite batholith, middle part of Nanling Range, South China. Sci. China. Ser. D Earth Sci. 52 (09), 1279–1294.